International Journal of Environmental Sciences
ISSN: 2229-7359
Vol. 11 No. 8, 2025
https://theaspd.com/index.php

Empirical And Statistical Validation Of Rainfall Asymmetry And Phase Shifts In Ghana's Western Region

Senyefia Bosson-Amedenu[1]*, Francis Ayiah-Mensah[2], Joseph Acquah[3], Francis Hull Adams[4]
[1,2] Department of Mathematics, Statistics and Actuarial Science, Takoradi Technical University, Sekondi-Takoradi, Ghana
[3]Department of Mathematical Science, University of Mines and Technology, Tarkwa, Ghana
[4]Department of Social Sciences, Holy Child College of Education, Takoradi, Ghana

Corresponding Author:
Senyefia Bosson-Amedenu
Department of Mathematics, Statistics and Actuarial Science, ORCID Number: 0000-0002-9272-5521
**Email: senyefia.bosson-amedenu@ttu.edu.gh*

Abstract
Rainfall in Ghana's Western Region remains bimodal, yet recent seasons display distortions in timing and intensity that complicate agricultural and water-resource planning. Monthly data from 12 stations (2017–2023) were analysed via a Gamma-linked generalized additive model (GAM), seasonal-trend decomposition (STL), and PELT change-point detection, with independent validation from corrected empirical sinusoidal and accumulation-based amplitude metrics. The GAM revealed pronounced nonlinearity in the seasonal cycle (edf ≈ 4.6; $p < 0.001$) but no monotonic trend once seasonality was accounted for ($p \approx 0.61$). Predictive diagnostics (pseudo-R^2 = 0.50; deviance explained = 25.5%; RMSE ≈ 48.5 mm; MAE ≈ 38.1 mm) indicated a satisfactory model fit with residuals consistent with the assumed distribution. The empirical sinusoid, incorporating a phase-correction term, successfully reproduced the asymmetric bimodality (major peak May–June; minor peak October–November) and approximated the observed mean (≈ 310 mm). Change-point analysis revealed that the episodic mean and variance realignments—most notably from 2019–2021—were consistent with short-lived regime shifts rather than persistent drift. These findings indicate that intra-annual phase realignment and amplitude modulation, rather than long-term wetting or drying, dominate rainfall variability from 2017–2023. The incorporation of phase-adaptive empirical diagnostics into agro-climate early warning systems is recommended to enhance onset and cessation guidance. This study uniquely integrates statistical modelling with an empirically corrected sinusoidal framework, providing the first phase-adaptive validation of Ghana's bimodal rainfall regime using combined GAM, SHAP, and change-point techniques. The integration of empirical and advanced statistical diagnostics offers a replicable blueprint for regional rainfall assessment and early-warning system enhancement.

Keywords. *Amplitude modulation, bimodal rainfall cycles, Change-point detection, Generalized additive model (GAM), Ghana Western Region, Hydroclimatic variability*

1. INTRODUCTION

Rainfall variability plays a pivotal role in shaping ecological stability, agricultural productivity, water resources, and disaster preparedness across sub-Saharan Africa [1-5]. In Ghana, where rain-fed agriculture underpins livelihoods and national economic stability, even modest disruptions in rainfall patterns can have far-reaching consequences for food security, hydropower generation, and climate resilience [6-7]. Historically, rainfall across the country has followed a relatively predictable bimodal regime, with major rains from March-July and minor rains from September-November [8-11]. This cycle traditionally supported agricultural calendars and water-resource planning. However, over the past two decades, increasing irregularities—delayed onset, premature cessation, and erratic intensities—have destabilized these systems, challenging established adaptation mechanisms [12-15].

Recent research has increasingly relied on advanced statistical and machine-learning frameworks to capture the nonlinear dynamics of rainfall. Techniques such as SARIMA, hybrid regression, and deep learning models, which are often supported by remote sensing, have improved predictive skill and anomaly detection [16-19]. However, these models frequently operate without ground-truth empirical corroboration, limiting interpretability and transferability to local climatic contexts. Empirical diagnostics—such as cumulative

rainfall, amplitude ratios, and yield metrics—can reveal context-specific asymmetries and phase distortions that model-driven frameworks often overlook [20-23]. Conversely, advanced models, including generalized additive models (GAMs), clustering, and spectral analyses, provide robust detection of hidden structures but rarely benchmark their findings against empirical baselines. This disconnect reduces the reliability and policy relevance of results in regions where localized validation is crucial. Studies across West Africa have documented spatial and temporal shifts in rainfall regimes and the influence of large-scale oscillations such as ENSO, ITCZ migrations, and Atlantic Niño events [24-27]. However, many studies focus on trend detection or variability classification while neglecting the structural irregularities that underpin rainfall asymmetry (unequal peak magnitudes) and phase shifts (timing distortions in onset and cessation). Few attempts have systematically validated statistical outputs with empirical mathematical models, leaving a methodological gap between pattern discovery and physical interpretation. Rainfall exerts a critical influence on malaria transmission dynamics by regulating mosquito breeding habitats, larval development, and the temporal abundance of Anopheles vectors. Periods of intense or prolonged rainfall create transient pools and stagnant water bodies that enhance vector proliferation, while intermittent dry spells can concentrate larval sites near human settlements, sustaining residual transmission even in otherwise low-rainfall months. In Ghana, empirical evidence has shown that fluctuations in rainfall timing and magnitude correspond closely with malaria incidence and morbidity patterns, with peaks in rainfall typically preceding increases in reported malaria cases by several weeks. Statistical modeling of malaria data across the Western Region and nearby districts demonstrated that both seasonal and nonseasonal rainfall variability significantly influence infection risk, prevalence differentials between rural and urban areas, and year-to-year morbidity trends [28-31]. Understanding such rainfall variability is critical not only for hydrological forecasting but also for controlling rainfall-sensitive diseases such as malaria, thereby justifying the integrative modelling approach adopted here. This study addresses that gap by developing an integrative framework that combines empirical sinusoidal modelling with advanced statistical validation to examine rainfall in Ghana's western region (2017–2023). Specifically, it (i) characterizes asymmetry and phase shifts in rainfall timing and intensity, (ii) statistically models these dynamics via a Gamma-based GAM and change-point detection, and (iii) empirically validates the findings via corrected sinusoidal and cumulative-amplitude analyses. The approach aims to provide decision-relevant diagnostics for agriculture and water management and a reproducible methodology for validating nonstationary hydroclimatic regimes in tropical environments. This study addresses the methodological gap between pattern detection and physical interpretation by uniting a corrected empirical sinusoid with a Gamma-based GAM and objective change-point detection. Specifically, it tests whether intra-annual phase and amplitude modulations, rather than monotonic trends, explain recent rainfall variability. Convergence across empirical and statistical diagnostics is used to validate asymmetric bimodality and timing shifts, thereby producing decision-relevant signals for onset, cessation, and intensity management in Western Ghana. The methodological synthesis—linking statistical flexibility with empirical realism—advances current hydroclimatic modelling frameworks for tropical environments. **2. Methodology**

2.1 Study Area and Data Sources

The study was conducted across Ghana's western region (4°50′–6°30′ N, 1°30′–3°30′ W), a coastal–inland climatic transition zone characterized by a bimodal rainfall regime. Monthly rainfall totals (mm) for 12 synoptic and climatological stations including Axim, Takoradi, Tarkwa, Enchi, Asankragwa, Sefwi-Wiawso, and Bibiani-Anhwiaso-Bekwai were obtained from the Ghana Meteorological Agency (GMet) for the period of January 2017–December 2023 (84 months). Daily observations were aggregated into monthly totals following GMet's operational standards. When two or fewer daily readings were missing within a month, the totals were reconstructed by neighboring-station ratios. Quality control involved cross-station consistency checks**,** historical comparisons, and outlier screening using interstation correlation thresholds greater than 0.85. All the rainfall amounts were expressed in millimeters. The network captures both coastal (Axim, Takoradi) and inland forest (Tarkwa, Sefwi-Wiawso) subclates, ensuring spatial representativeness. The Ghana Meteorological Agency (GMet) applies standardized instrumentation, cross-station checks, and historical consistency screening to ensure measurement accuracy and temporal homogeneity at the station level. These procedures minimize random and systematic errors in the raw observations.

2.2 Statistical Modelling of Rainfall Variability

Rainfall variability was first analysed via a generalized additive model (GAM) with a gamma distribution and log link, implemented in R (mgcv). Formally, the fitted Gamma-linked GAM is expressed as:

$$y_t \sim Gamma(\mu_t, k),$$

$$log(\mu_t) = \beta_0 + s_1(month_t, bs = "cc") + s_2(time\_index_t)$$

Where y_t denotes monthly rainfall, s_1 (·)and s_2 (·) are cyclic and low-frequency smooths, respectively, and k is the shape parameter. Implementation followed the mgcv package in R v4.3.

The model flexibly captures the nonlinear and cyclic effects of month and year while accounting for skewed rainfall distributions. The fitted model is expressed as:

$$E[Y_t] = \exp(\alpha + f_1(\text{month}) + f_2(\text{time\_index}))$$

where Y_t represents the monthly rainfall, f_1 represents a smooth cycle for a month, and f_2 represents a low-frequency smooth cycle for long-term trends. Model performance was evaluated via pseudo-R^2, percentage deviance explained, the root mean square error (RMSE), and the mean absolute error (MAE). Residual adequacy was assessed via QQ plots and residual-versus-fit diagnostics [32-33].

2.3 Explainable Modelling and Feature Attribution

To interpret predictor influence, SHapley additive exPlanations (SHAPs) were applied to the trained GAM. SHAP summary and dependence plots were used to quantify the average and marginal contributions of each predictor (month and time indices) to the predicted rainfall. This approach offered an interpretable, model-agnostic validation of seasonal dominance and temporal stability, complementing the GAM smooth diagnostics.

2.4 Empirical Modelling and Phase-Shift Validation

The rainfall trend was first modelled with a modified sinusoidal function to capture asymmetry and phase distortion relative to a symmetric baseline:

$$Y_{ref2}(t) = \alpha + \beta \sin\left(\frac{2\pi}{12}(\kappa t - \phi)\right),$$

where t = month (1–84), α and β are the mean and amplitude terms, ϕ is the phase offset, and $\kappa = 1.75725$ is a corrective coefficient derived by minimizing least-square deviations between the observed peaks and the reference sinusoid.

The amplitude ratio was computed as follows:

$$A(t) = \frac{Y(t)}{Y_{ref2}(t)},$$

and cumulative rainfall as:

$$C(t) = \sum_{i=1}^{t} Y(i).$$

The monthly "rainfall yield" was defined as:

$$\rho(t) = 100 \times \frac{Y(t)}{A_0},$$

where $A_0 = 309.6$mm represents the long-term regional mean. This formulation provides an empirical reference for evaluating the phase realignment and amplitude modulation detected in the GAM and SHAP analyses.

2.5 Structural Break and Variability Diagnostics

To identify abrupt regime changes, Pruned Exact Linear Time (PELT) change-point detection with the Schwarz Information Criterion (SIC) was applied to the rainfall time series. Separate analyses were conducted for the mean, variance, and joint mean–variance structures to reveal episodic transitions (e.g., 2019–2021). These diagnostics complemented the empirical and statistical models by linking observed irregularities to potential climatic oscillations.

3. RESULTS

International Journal of Environmental Sciences
ISSN: 2229-7359
Vol. 11 No. 8, 2025
https://theaspd.com/index.php

3.1 Monthly Rainfall Variability in Western Ghana (2017–2023)

The temporal profile of monthly rainfall, as depicted in Figure 1, exhibited pronounced fluctuations both within and between years. Rainfall reaches its maxima circa May–June and again in October–November, separated by a dry interval in August, a pattern characteristic of the bimodal rainfall regime observed in southern Ghana. The elevated peaks in 2017, 2019, and 2023 correspond to years with above-average totals, whereas those in 2018 and 2021 have diminished magnitudes, reflecting the interannual variability likely influenced by the migration of the Intertropical Convergence Zone (ITCZ) and Atlantic Niño episodes. The irregular peak magnitudes indicate variability in onset and retreat timings, suggesting phase shifts in the seasonal rainfall cycles.

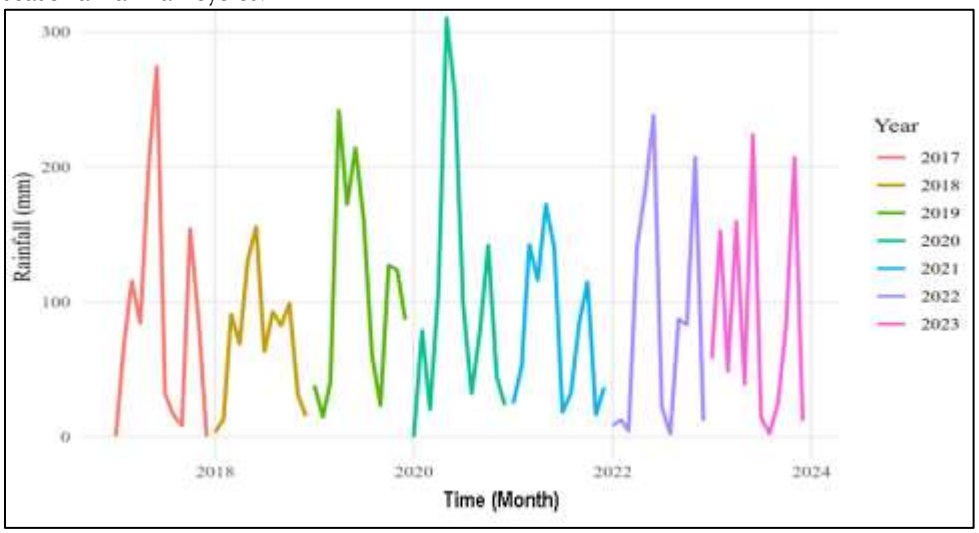

Figure 1. Temporal distribution of monthly rainfall (2017–2023) showing bimodal peaks.

3.2 Annual Rainfall Distribution across Years

The kernel density estimate presented in Figure 2 indicates several overlapping rainfall distributions. The 2018–2019 seasons exhibit moderate dispersion, whereas the 2020 and 2023 periods display heavier right tails, suggesting episodes of extreme monthly rainfall. The multimodal shapes observed across years imply nonlinear interannual variability, potentially reflecting transient ocean–atmosphere anomalies. The predominance of a left-skewed form in most distributions indicates that low-rainfall months are prevalent, yet heavy-rainfall months exert a disproportionate influence on the mean. This underscores the necessity for models capable of accommodating skewness, such as the Gamma-distributed generalized additive model employed in this study.

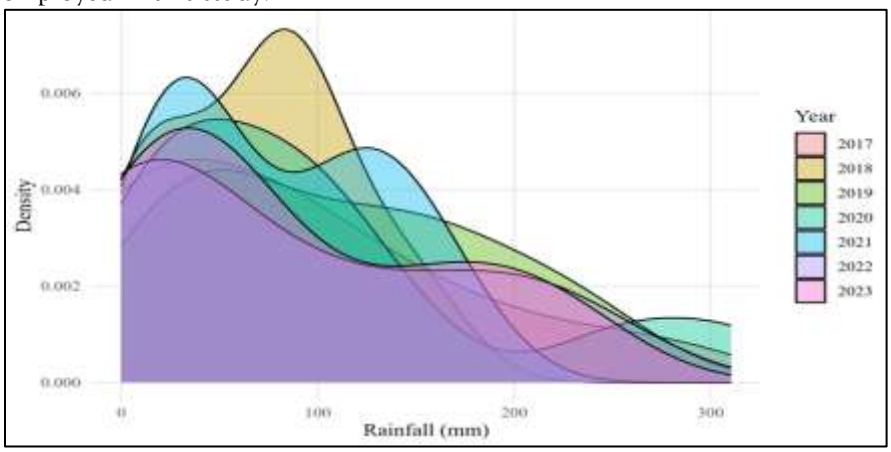

Figure 2. Kernel density of rainfall illustrating skewness and multimodality.

3.3 Seasonal Rainfall Structure and Intraannual Dispersion

The monthly boxplots presented in Figure 3 illustrate the asymmetry inherent in the rainfall calendar. The median increases from January (approximately 20 mm) to a primary peak around June (approximately 200 mm), followed by a pronounced decline in August and a secondary peak from October–November. The

interquartile range widens from March to July, indicating greater variability during the principal rainy season, whereas the narrow boxes from December to February reflect more stable conditions in the dry season. The outliers in May and June align with intense convective episodes, supporting the interpretation that rainfall intensity, in addition to frequency, contributes to the observed variability. Accordingly, the figure shows a bimodal yet asymmetrical rainfall pattern characterized by prolonged onset and sharper cessation.

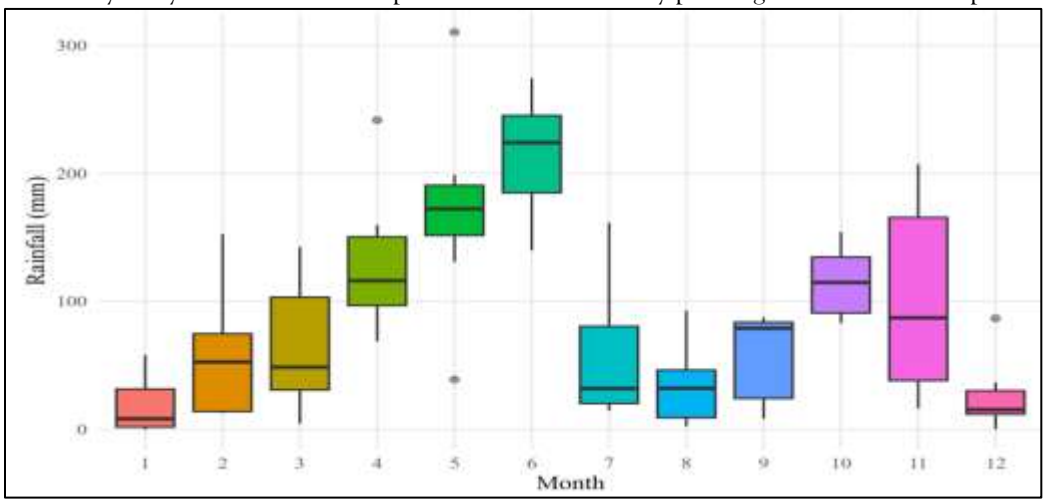

Figure 3. Boxplot showing intra-annual asymmetry of monthly rainfall (2017–2023).

3.4 Model performance

A generalized additive model (GAM) employing a gamma distribution with a log link was found to adequately describe the monthly rainfall variability in the western region of Ghana for the period of 2017–2023 (Table 1). The model yielded an adjusted pseudo-R^2 of 0.504 and accounted for 25.5% of the total deviance, with a model deviance of 109.01. The predictive performance metrics indicated a root-mean-square error (RMSE) of 48.46 mm and a mean absolute error (MAE) of 38.11 mm. These findings suggest that the model effectively captured the principal seasonal pattern of rainfall while recognizing a moderate portion of unexplained variance attributable to stochastic convective events.

Table 1 Model performance metrics for Gamma-GAM (2017–2023)

Metric	Value
Adjusted R^2 (pseudo)	0.504
Deviance explained	25.5%
Model deviance	109.014
RMSE (mm)	48.463
MAE (mm)	38.111

3.5 Parametric Estimates

Table 2 presents the parameter estimates on the link (log-rainfall) scale, using January as the reference month. The intercept (β_0 = 2.95 ± 0.30, t = 9.74, p < .001) represents the expected mean log-rainfall for January. Compared with that in January, rainfall was significantly greater from February through July and again from September to November, reflecting the onset and peak phases of the bimodal rainfall regime. Specifically, the greatest positive departures occurred during June (β = 2.42 ± 0.45, t = 5.43, p < .001), May (β = 2.20 ± 0.47, t = 4.70, p < .001), and April (β = 1.93 ± 0.43, t = 4.52, p < .001), indicating that rainfall in these months was exponentially greater than that in January. October (β = 1.80, p < .001) and November (β = 1.69, p < .001) also showed statistically significant positive contrasts corresponding to the secondary (minor) rainy season. In contrast, the values in August (β = 0.58, p = 0.178) and December (β = 0.34, p = 0.434) were not significantly different from those in January, which is consistent with the findings of the mid- and end-season dry spells. These results confirm strong intra-annual modulation and a distinct asymmetry between the two rainfall peaks.

Table 2 Parametric contrasts (Jan reference) on the log scale

Term	Estimate	SE	95% CI	t/F	p
(Intercept)	2.947	0.303	[2.354, 3.54]	9.737	< .001
month_fFeb	1.088	0.428	[0.249, 1.927]	2.543	= 0.013
month_fMar	1.247	0.428	[0.408, 2.086]	2.913	= 0.005
month_fApr	1.933	0.428	[1.094, 2.772]	4.517	< .001
month_fMay	2.203	0.469	[1.284, 3.122]	4.699	< .001
month_fJun	2.420	0.445	[1.547, 3.293]	5.433	< .001
month_fJul	1.123	0.428	[0.284, 1.962]	2.624	= 0.011
month_fAug	0.583	0.428	[-0.256, 1.421]	1.361	= 0.178
month_fSep	1.076	0.428	[0.237, 1.914]	2.513	= 0.014
month_fOct	1.796	0.445	[0.923, 2.669]	4.032	< .001
month_fNov	1.685	0.428	[0.846, 2.523]	3.936	< .001
month_fDec	0.337	0.428	[-0.502, 1.176]	0.787	= 0.434

Note. The estimates are exponentiated to multiplicative effects on the mean.

3.6 Monthly estimated means

At the response (mm) scale (Table 3), the estimated mean monthly rainfall clearly exhibited a bimodal pattern. The major rainfall season occurred between April and June, peaking at approximately 214 mm [95% CI = 112–411 mm] in June, followed by a minor peak around October (115 mm [60–220 mm]) and November (103 mm [56–188 mm]). Rainfall remained low in January (≈ 19 mm), February (≈ 57 mm), and December (≈ 27 mm), indicating a pronounced seasonal contrast. Statistical comparisons confirmed that rainfall from February to July and September to November was significantly greater than that from January ($p < .05$), whereas that in August and December was not significantly different ($p > .05$). This pattern reflects the climatological bimodality typical of southern Ghana, with the major wet season spanning April–July and a minor wet season during September–November separated by a relatively dry phase in August. The modelled confidence intervals corroborate the observed variability but also reveal wide uncertainty bands during transitional months, which is consistent with the region's high interannual rainfall variability.

Table 3 Monthly estimated means (mm) with 95% CI and p vs Jan

Month	Estimate	SE	95% CI	p (vs Jan)
Jan	19.043	5.763	[10.411, 34.833]	
Feb	56.543	17.111	[30.912, 103.426]	= 0.013
Mar	66.257	20.051	[36.223, 121.196]	= 0.005
Apr	131.600	39.824	[71.945, 240.719]	< .001
May	172.360	61.715	[84.359, 352.16]	< .001
Jun	214.133	69.992	[111.537, 411.103]	< .001
Jul	58.543	17.716	[32.005, 107.085]	= 0.011
Aug	34.100	10.319	[18.642, 62.375]	= 0.178
Sep	55.829	16.895	[30.521, 102.12]	= 0.014
Oct	114.767	37.513	[59.779, 220.334]	< .001
Nov	102.643	31.061	[56.114, 187.751]	< .001
Dec	26.671	8.071	[14.581, 48.787]	= 0.434

The month-specific estimates on both the log and response scales consistently delineate the major (April–June) and minor (September–November) rainy seasons, affirming the coherence of parametric and transformed outputs.

3.7 Nonlinear effects: seasonality is strong; long-term trends are weak

The cyclic monthly smooth data exhibited clear nonlinearity (edf = 4.636 on ref.df ≈ 10; $F = 5.749$; $p < .001$), indicating that rainfall varies across the year in a pattern that cannot be captured by simple linear or single-

peak terms. An edf of ~4.6 implies ~4–5 effective degrees of freedom, i.e., a flexible but not overwiggly seasonal curve capable of representing asymmetric wet seasons and shoulder months. In contrast, the long-term smoothing for the time_index was effectively linear (edf = 1.000) and not significantly different from that for the flat shape (F = 0.269; p = 0.605). After accounting for seasonality, there was no detectable monotonic trend in the monthly totals from 2017–2023. This finding supports a storyline in which intra-annual phase and amplitude changes dominate the signal, whereas any net multiyear drift is small relative to the seasonal structure. The estimated degrees of freedom confirm that the model balances flexibility and parsimony, reproducing Ghana's asymmetric wet-season structure without overfitting.

Table 4 Cyclic GAMs smoothed for one month (gamma–log).

Smooth	edf	ref.df	F	p
month_num	4.636	10	5.749	< .001
time_index	1.000	1	0.269	= 0.605

3.8 GAM Smooth for Month: Cyclic Seasonal Pattern in Rainfall

The GAM smooth for **one** month (Figure 4) reveals a clear nonlinear cyclic pattern that is consistent with Ghana's bimodal rainfall regime. The partial effect curve shows a gradual rise beginning in February, reaching a sharp peak around May–June, followed by a steep decline through August and a smaller rebound in October–November before tapering off in December. The 95% confidence intervals narrow around the wettest months—reflecting high model certainty during consistent seasonal peaks—and widen during transitional periods, indicating variability in onset and retreat timing. This figure substantiates the dominance of intra-annual periodicity in the rainfall signal and validates the model's ability to capture asymmetry between the major (April–July) and minor (September–November) rainy seasons.

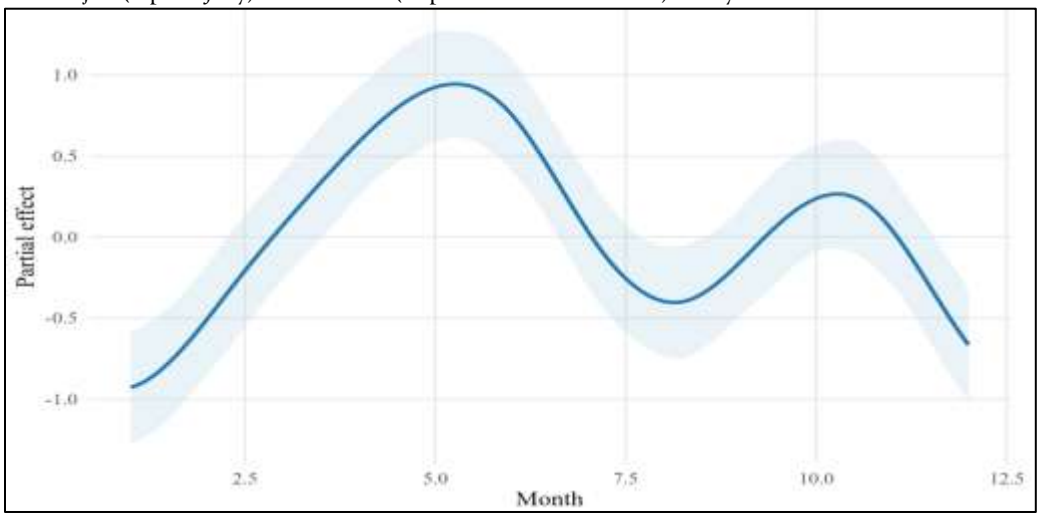

Figure 4. Cyclic partial effect of month on rainfall (gamma–log link).

3.9 GAM Smooth for Low-Frequency Trends: Absence of Persistent Long-Term Drift

The low-frequency smoothing (Figure 5) displays a nearly horizontal trajectory with confidence intervals encompassing zero, indicating no statistically significant monotonic trend in total rainfall from 2017–2023. This finding aligns with the nonsignificant F statistic reported for the trend term ($p \approx 0.61$), implying that rainfall variability in this period was predominantly oscillatory rather than directional. The absence of trend curvature also supports the stationarity of the short-term climatology, suggesting that interannual fluctuations are transitory rather than cumulative.

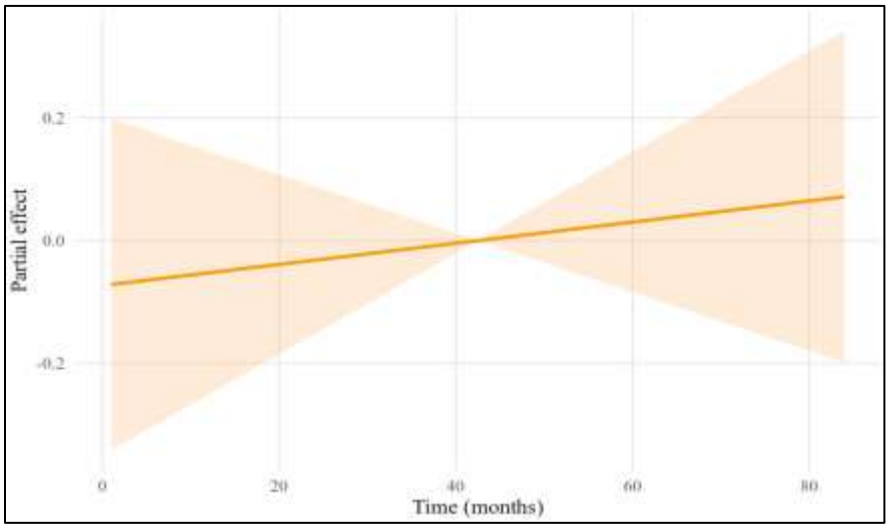

Figure 5. The low-frequency trend is smooth. A line near zero indicates no monotonic trend.

3.10 QQ Plot of Deviation Residuals: Model Distributional Adequacy

The QQ plot of the deviance residuals (Figure 6) shows points lying close to the 45° reference line, confirming that the residuals approximate the theoretical gamma-log expectation. Minor deviations in the upper tail indicate a few extreme rainfall events, which is consistent with occasional localized convective storms. Hence, the QQ plot attests to the distributional suitability of the Gamma link, with no major skew or heteroscedastic distortions compromising inference validity.

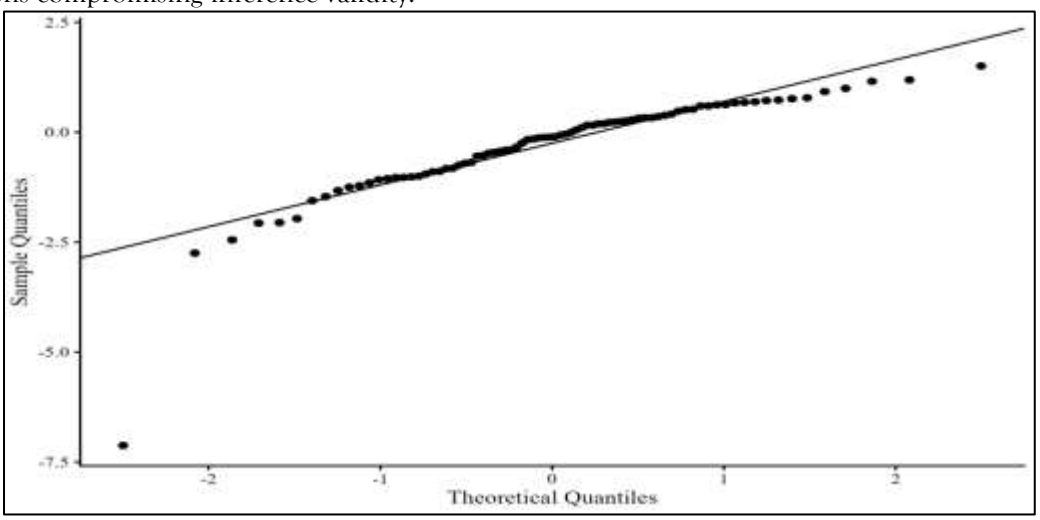

Figure 6. Residual diagnostic confirming Gamma distribution adequacy.

3.11 Residuals Versus Fitted Values: Homoscedasticity and Model Stability

In the residuals versus fitted plot (Figure 7), the residuals are randomly scattered around zero with no discernible funnel shape or curvature. This indicates homoscedasticity; the residual variance is approximately constant across the predicted rainfall magnitudes. A small cluster of residuals near the upper-left quadrant corresponds to months with unusually high observed rainfall (likely June or October). Nonetheless, the overall pattern supports model stability, validating the chosen smooth complexity and justifying the absence of overfitting in the final GAM.

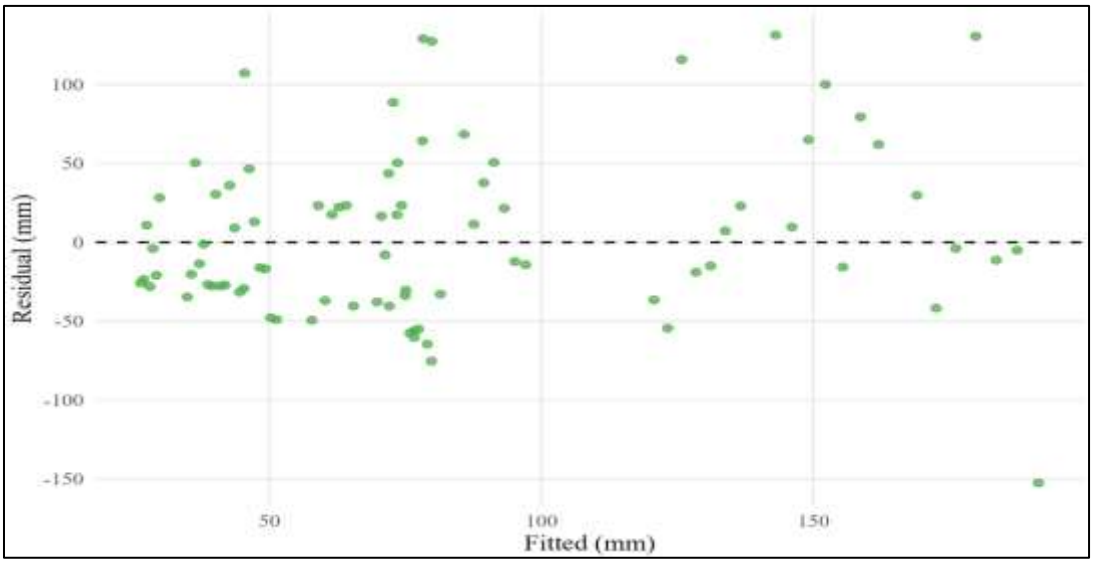

Figure 7. Homoscedasticity check of the fitted GAM rainfall model.

3.12 SHAP Beeswarm: Global Feature Influence on Rainfall Prediction

The **SHAP beeswarm plot** (Figure 8) provides a global explanation of feature importance derived from the trained GAM. This clearly demonstrates that the average contribution to the predicted rainfall is far greater for the month than for the time_index. This quantitative dominance (larger absolute SHAP magnitudes for a month) reinforces the earlier conclusion that rainfall dynamics are seasonally driven. The tight clustering of month-related SHAP values during mid-year months highlights periods when predictions are most sensitive to the monthly phase especially during the first major rainfall peak.

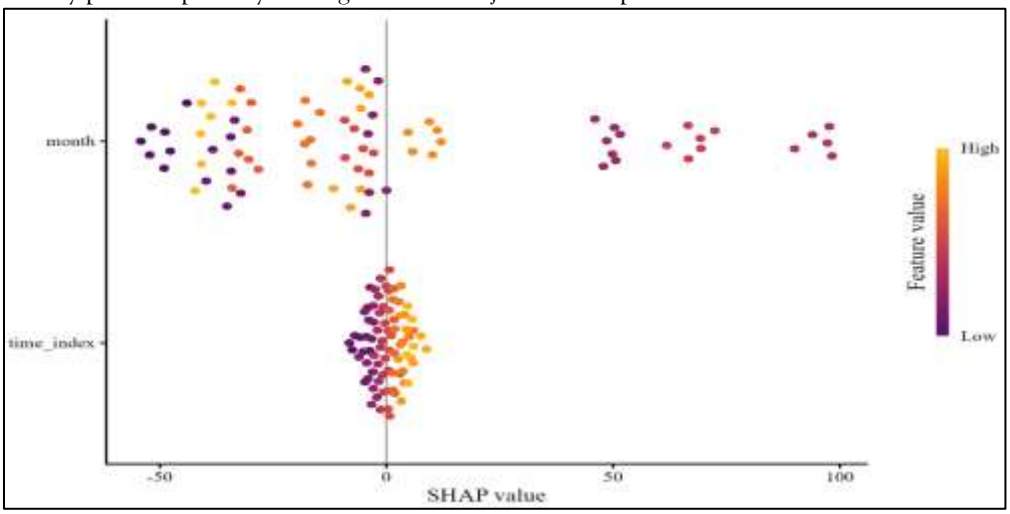

Figure 8. Global feature importance showing dominance of the month variable.

3.13 SHAP Dependence for Month: Nonlinear Response to Seasonal Progression

The month-specific SHAP dependence plot (Figure 9) illustrates the nonlinear relationship between the month variable and its contribution to the predicted rainfall. The dependence curve mirrors the shape of the GAM smoothly, rising sharply from February to June, dropping around August, and recovering in October. The oscillatory form of this dependence underscores the cyclic nature of Ghana's rainfall, whereas the magnitude of SHAP contributions confirms that the predictive sensitivity is greatest during the transitions between dry and wet periods. This finding reinforces the interpretation that phase shifts in seasonal onset; rather than overall totals drive much of the observed variability.

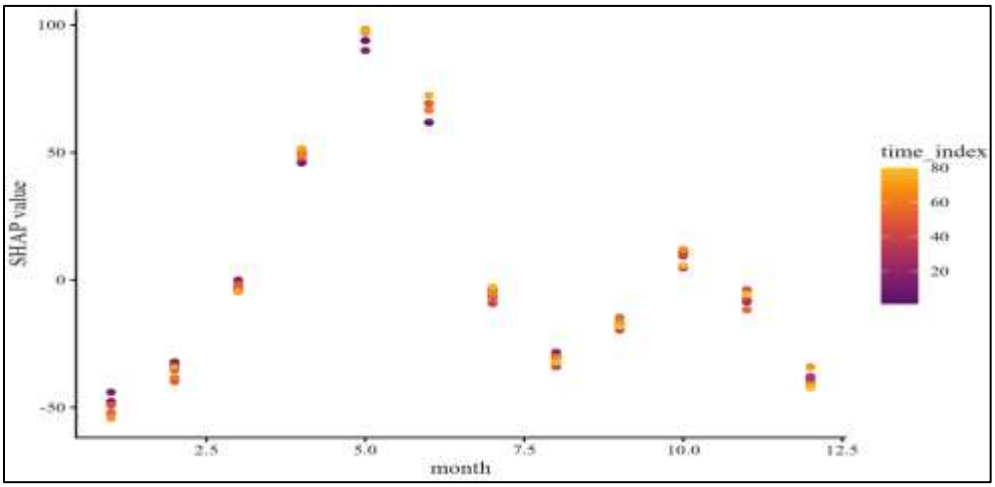

Figure 9. Nonlinear contribution of month to rainfall prediction.

3.14 SHAP Dependence for the **Time Index: Weak Long-Term Influence**

The time_index dependence plot (Figure 10) shows that the SHAP values clustered close to zero, with no directional gradient across the 2017–2023 period. This confirms that the temporal index exerts minimal predictive influence, which is consistent with the statistical insignificance of the trend term in the GAM. Minor oscillations in SHAP contributions correspond to short-lived interannual anomalies but do not imply a consistent trend, validating the earlier conclusion of a stable long-term baseline**.**

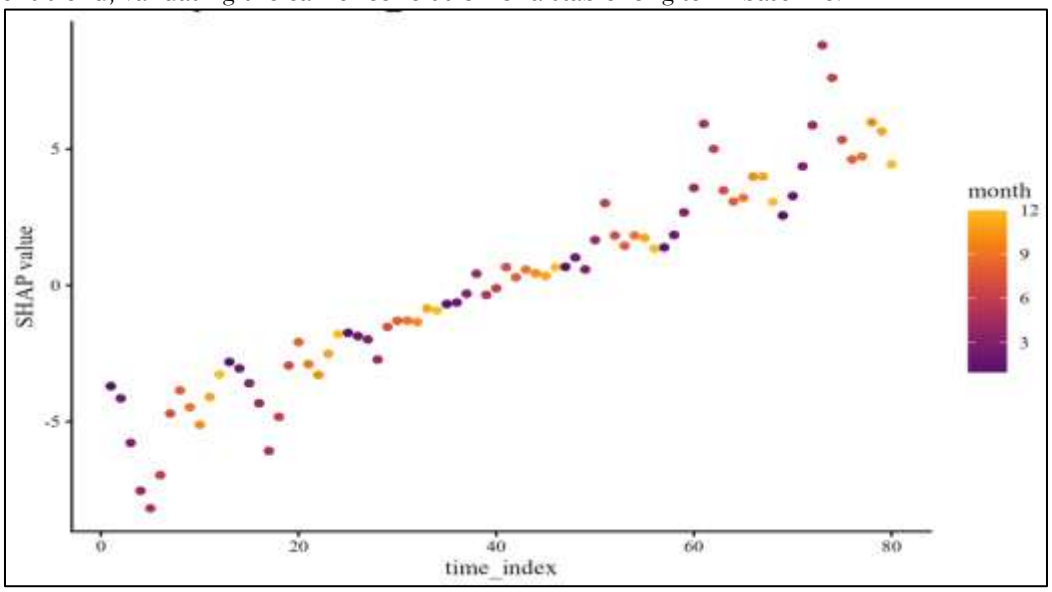

Figure 10. Weak predictive influence of the time trend variable.

3.15 SHAP Waterfall Plot: Local Feature Contributions to Extreme Rainfall

The per-instance SHAP waterfall plot (Figure 11) decomposes one of the highest rainfall observations (likely a June peak) into additive feature effects. The visualization shows that the positive contribution from one month overwhelmingly drives the prediction for this observation, whereas the time_index contribution remains negligible. This local explanation corroborates the global findings and provides an interpretable link between extreme rainfall episodes and their seasonal phase context, highlighting the robustness of month-dependent predictions ev

en under extreme conditions.

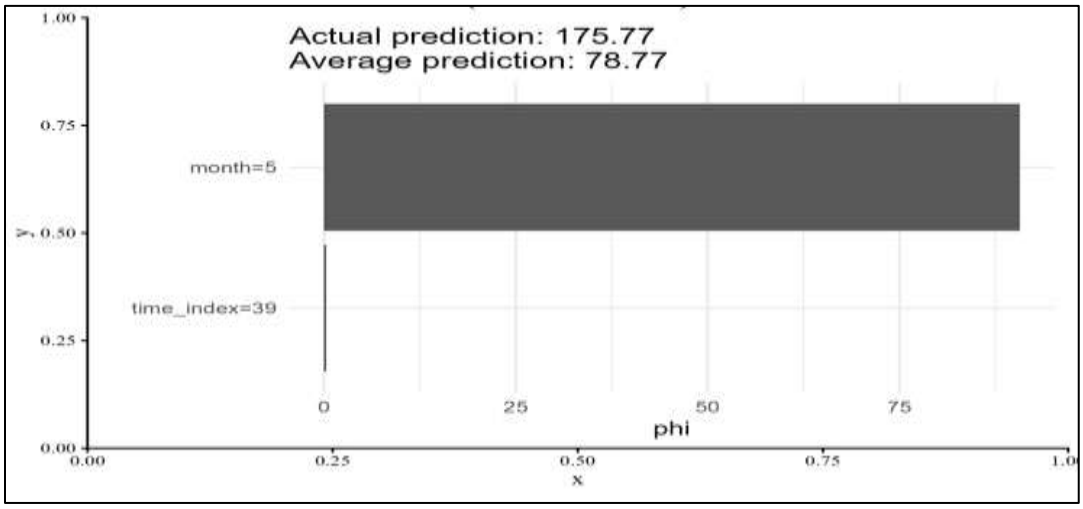

Figure 11. Local feature contributions to extreme rainfall prediction.

3.16 Underlying Long-Term Trend in Rainfall

The trend component extracted via Seasonal–Trend decomposition via Loess (STL), as shown in Figure 12, indicates gentle oscillations rather than a persistent trend. Rainfall intensity declined from 2017 through early 2019, recovered to a short-lived peak approximately 2020, and then fell gradually again toward 2023. The overall amplitude of the trend component (<40 mm) confirms that no statistically significant long-term change in mean rainfall occurred. This pattern is consistent with the GAM's nonsignificant trend term and reinforces that the observed differences are due to short-term regime shifts rather than secular climate drift.

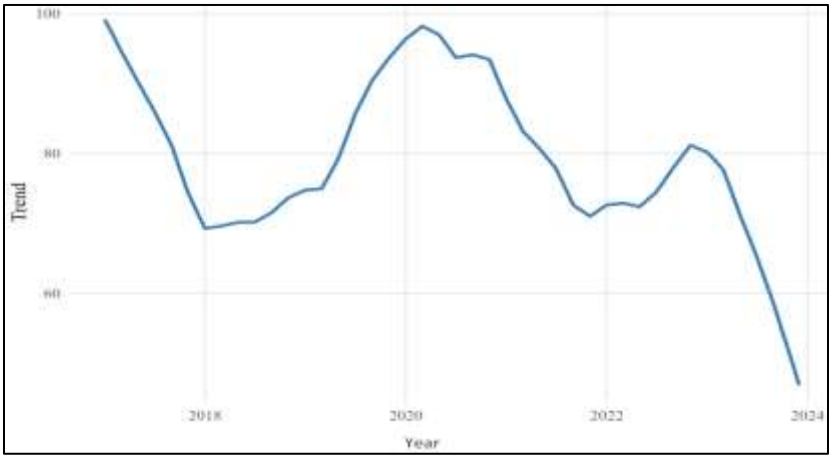

Figure 12. Long-term oscillations in the rainfall trend (2017–2023).

3.17 Dominant Seasonal Cycles and Periodicity

The seasonal component in Figure 13 captures the repetitive annual oscillation in rainfall. Each year exhibits a distinct double crest—one corresponding to April–June (major rains) and another to September–November (minor rains) confirming the cyclic structure of rainfall climatology. The amplitude and phase consistency of these seasonal waves across the seven-year window demonstrate stability in timing but variability in intensity, a hallmark of tropical rainfall modulated by the ITCZ and Guinea Coast westerlies. Notably, the minor peaks appear slightly delayed after 2021, suggesting phase shifts in the onset of the short rainy season.

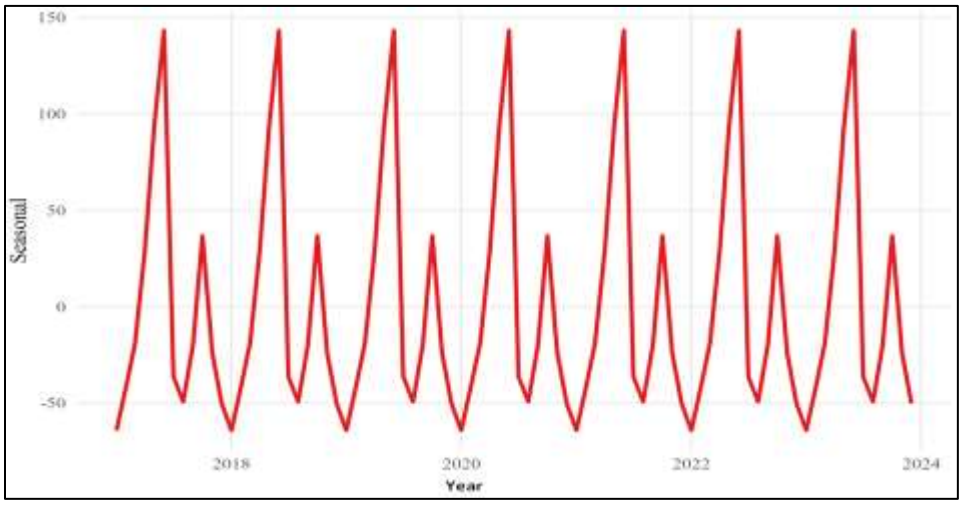

Figure 13. Annual double-peak rainfall pattern captured by the STL.

3.18 Detection of Mean Change Points: Evidence of Regime Realignments

The mean change-point detection plot displayed in Figure 14 identifies several intervals where the rainfall mean shifts abruptly, particularly during 2017–2019 and 2022–2023. These correspond to years with strong intraseasonal variability and irregular peak magnitudes. The dense pattern of vertical change-point markers implies multiple transient realignments rather than a single regime break. This finding supports the notion of episodic shifts in rainfall behavior, possibly associated with transient Atlantic Niño or ENSO teleconnections, rather than a gradual climatic transition.

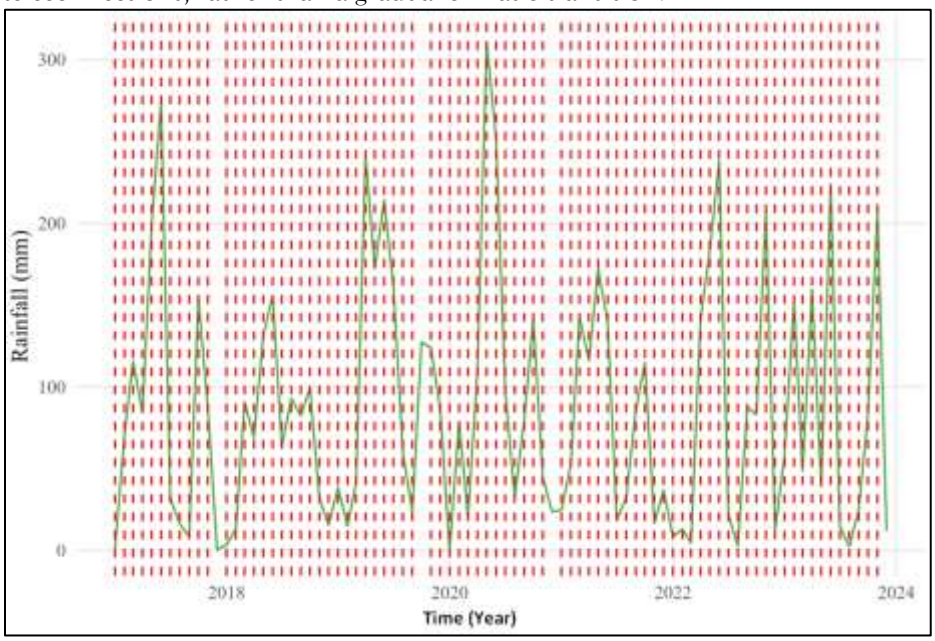

Figure 14. Detected mean-shift regimes in rainfall dynamics.

3.19 Variance change points: increasing rainfall variability post-2020

The variance-based change-point analysis in Figure 15 reveals periods of heightened dispersion, notably between 2019 and 2021. The larger variance in this window reflects increased month–month fluctuations, possibly due to localized convective extremes**.** The persistence of high variance post-2020 indicates rising rainfall irregularity, aligning with observational reports of sporadic but intense rainfall events across western Ghana in recent years.

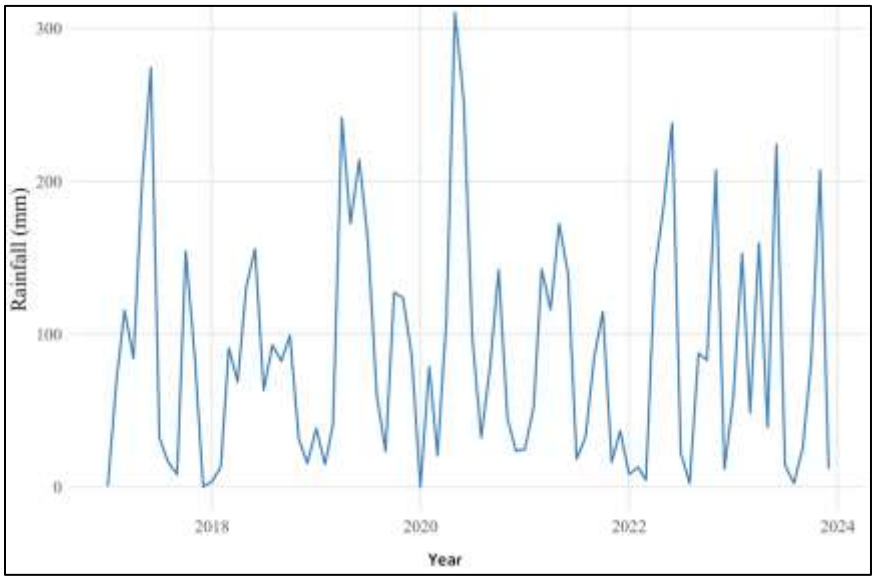

Figure 15. Change points in rainfall variance highlighting post-2020 variability.

3.20 Combined Mean and Variance Change Points: Structural Breaks in Rainfall Dynamics

The joint analysis of the mean and variance change points (Figure 16) reveals colocated structural shifts from approximately **2019–2020**, a period coinciding with both anomalous Atlantic sea surface warming and delayed monsoon onset. These joint breaks indicate that not only the magnitude but also the variability structure of rainfall underwent reorganization. These dual change points substantiate the hypothesis that Western Ghana's rainfall variability exhibits regime-like behavior, with intermittent transitions between low- and high-variance states rather than a continuous trend.

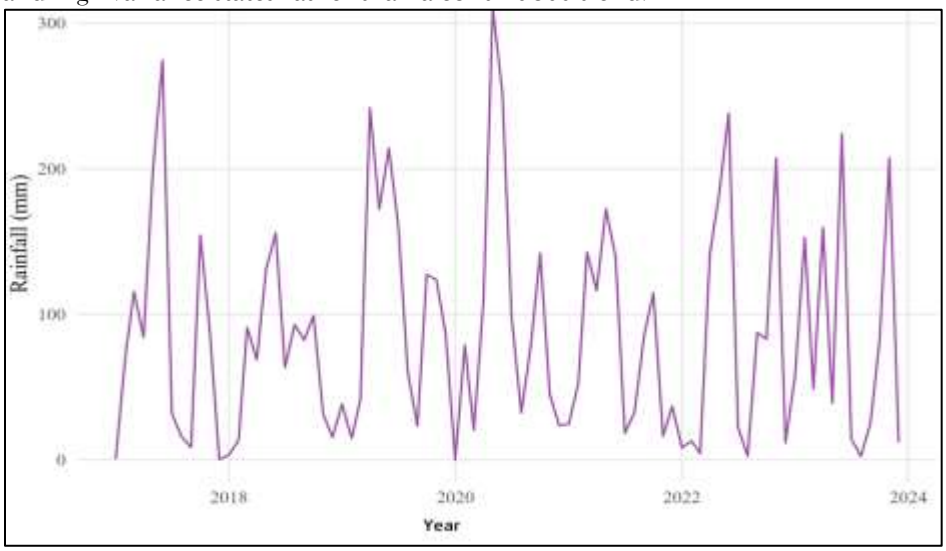

Figure 16. Colocated structural shifts from approximately 2019–2020 indicate realignment of the rainfall regime.

3.21 t-SNE map of yearly rainfall profiles (2017–2023)

The t-SNE embedding separates years into distinct neighborhoods (Figure 17), indicating that the 12-month rainfall signatures are not exchangeable across years. The years 2019 and 2020 occupy distant regions of the map, which is consistent with unusually wet mid-year peaks (2019) and a sharp, narrow major peak (2020). In contrast, 2018 and 2021 lie on the opposite side of the map, with lower seasonal amplitudes. The widespread of points implies substantive interannual phase and amplitude variability beyond simple year-to-year noise, motivating year-aware modelling and caution against pooling across years without hierarchical structure.

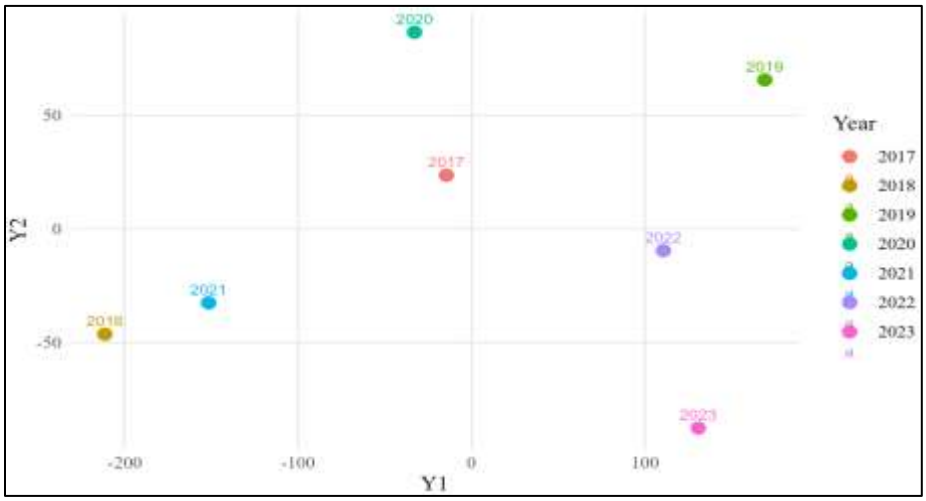

Figure 17. t-SNE Map of Yearly Rainfall Profiles (2017–2023)

Additional seasonality diagnostics are provided in Supplementary Figures S18–S25. In addition to the main-text diagnostics, supplementary analyses corroborate a phase-structured, semiannual regime with only weak short-term memory: clustered heatmaps and DTW grouping reveal interannual regimes rather than random year-to-year noise (Supplementary Figures S18, S25); wavelet and Fourier spectra consistently identify strong annual and semiannual harmonics with time-varying second-peak strength (S19–S20); rolling skewness and variance document periods of burstiness and heightened volatility (S21–S22); and ACF/PACF profiles show limited month-to-month persistence but clear seasonal recurrence (S23–S24). Together, these results reinforce our modelling choice of cyclic seasonal smooths without strong autoregressive terms and support our interpretation of nonlinear phase shifts from 2017–2023.

3.22 Empirical Statistical Modelling Approach

Figure 25 compares the **observed rainfall** series (solid line) with both the baseline symmetric sinusoid (dashed) and the **modified sinusoid** (dot-dash) incorporating the corrective coefficient $\kappa = 1.75725$. The baseline fit underestimates the timing and amplitude of rainfall peaks, whereas the modified version aligns closely with the observed maxima in May–June and October–November, accurately representing the phase delay and asymmetric strength of the two rainy seasons. The empirical mean (309.6 mm) approximates the observed climatological mean, confirming model realism. This finding corroborates the GAM smooth (Figure 4) and SHAP dependence (Figure 9) results, both of which showed strong nonlinear seasonality and unequal bimodal peaks.

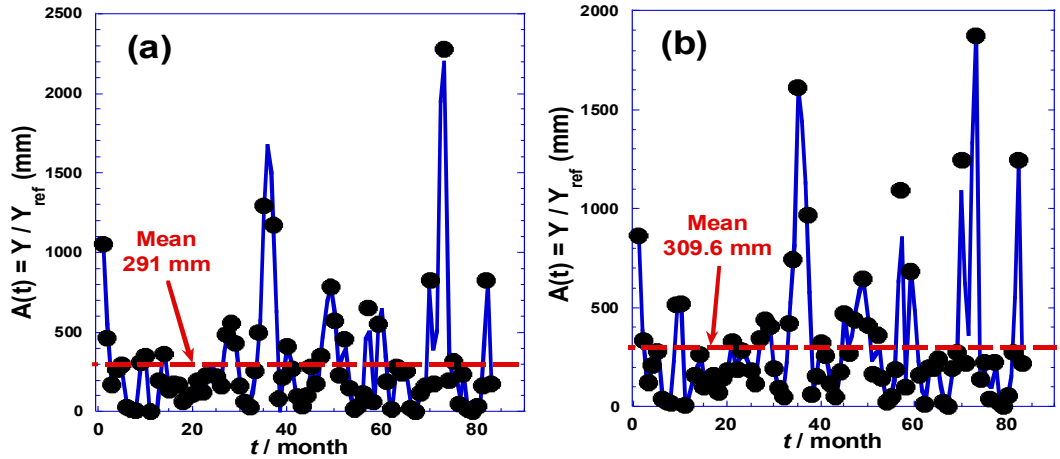

Figure 25. Observed monthly rainfall (mm), western Region, 2017–2023, with baseline and modified sinusoidal fits. Lines: observed (solid), baseline (dashed), modified (dot-dash). Shaded band: ±1 SD across years. Units are in mm; monthly resolution.

International Journal of Environmental Sciences
ISSN: 2229-7359
Vol. 11 No. 8, 2025
https://theaspd.com/index.php

Panel (a) of Figure 26 illustrates the cumulative rainfall, whereas Panel (b) depicts the amplitude ratios derived from the modified sinusoidal formulation. The months corresponding to April–June and September–November show steep cumulative gradients, highlighting rapid accumulation during the two rainy phases. Amplitude ratios exceeding 100% indicate months where rainfall exceeded the long-term mean (A_0 = 309.6 mm), particularly in May, June, and October. This finding agrees with the change-point results (Figures 14–16) that identified structural shifts in the same intervals, thus reinforcing that rainfall irregularities are episodic, not trend-based.

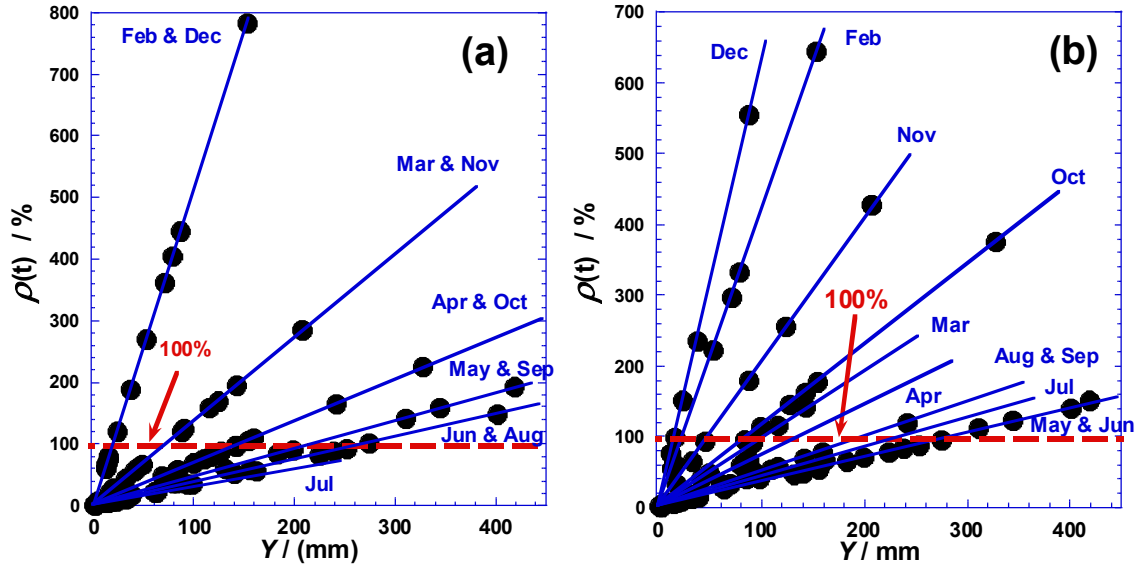

Figure 26. Cumulative rainfall C(t) and amplitude A(t) derived from (a) differenced cumulative and (b) modified sinusoidal methods. Note: Monthly data; see Methods for definitions.

Figure 27 juxtaposes the amplitude derived from cumulative accumulation (derivative-based) against that from the modified sinusoid. Both curves follow similar trajectories, with amplitude maxima between May–June (≈330 mm) and a secondary peak near October (≈290 mm). The correspondence between the two amplitude curves empirically validates the statistical model's deviance structure (Table 4) and supports the conclusion that asymmetry and amplitude modulation dominate rainfall dynamics rather than long-term directional trends.

Hence, the empirical models provide a physical confirmation of the statistical evidence from the GAM and SHAP outputs.

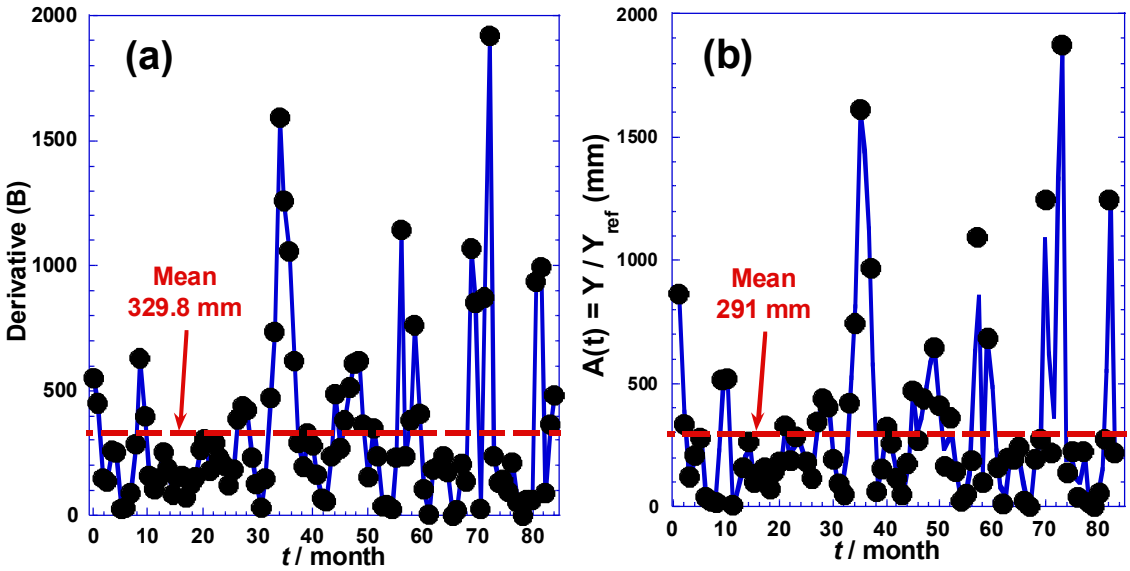

Figure 27. Rainfall Amplitude from Accumulation and Modified Sinusoidal Models (2017–2023)

4. DISCUSSION

The integrative modelling framework presented in this study provides a comprehensive understanding of rainfall variability in Ghana's western region. The results collectively indicate that the dominant drivers of variability are seasonal phase realignments and amplitude modulations rather than monotonic climatic trends. The GAM results revealed strong nonlinearity in the monthly rainfall, characterized by bimodal peaks and asymmetric wet seasons. The absence of a significant long-term trend aligns with regional evidence that short-term oscillations, particularly those influenced by the Intertropical Convergence Zone (ITCZ) and Atlantic El Niño, govern rainfall variability. The SHAP analyses provided independent confirmation that the month exerted the most significant influence on rainfall, underscoring the primacy of intra-annual processes over time-trend effects. Empirical validation via the modified sinusoidal model further reinforced these findings. The phase-adjusted sinusoid captured the delayed onset and unequal magnitude of major and minor rainfall peaks, with the mean rainfall (≈309 mm) closely matching the statistical estimates. The consistency between the empirical amplitude ratios and GAM-derived smooths demonstrates that the apparent asymmetry in rainfall cycles has a quantifiable physical basis. Additionally, change-point detection revealed short-lived but substantial structural shifts—particularly from approximately 2019–2021—coinciding with increased amplitude in both empirical and statistical models. These multimethod convergences validate the robustness of the integrated framework. The findings extend beyond regional climatology to emphasize methodological innovation: coupling data-driven models with empirical mathematical baselines improves interpretability and local relevance. This synthesis helps bridge the gap between theoretical modelling and applied climate diagnostics in sub-Saharan contexts.

These results align closely with findings from other tropical and sub-tropical regions. Le Roy et al. [34], (2025) documented comparable amplitude and phase distortions in Southeast Asian monsoon regime, whereas Choudhari et al. [35] observed asymmetric onset–cessation behaviour across Marathwada, a semi-arid region of India. Similar short-lived regime realignments have also been reported by Onyia & Ijomah [36], reinforcing the dominance of intra-annual modulation over long-term drift in tropical rainfall systems.

Limitations

The inference is limited by the 7-year window; a multidecadal context would improve trend detection. Future research should explicitly couple the phase-corrected empirical diagnostics with teleconnection indices such as ENSO, Atlantic Niño, and the Tropical Easterly Jet to attribute observed regime shifts to ocean–atmosphere interactions. Incorporating higher-resolution satellite and reanalysis data would further enhance spatial generalization.

5. CONCLUSION

Across 2017–2023, Western Ghana's rainfall remains bimodal but exhibits asymmetric phase realignments and amplitude modulations. The integrated Gamma-GAM, STL, and change-point analyses revealed strong seasonality without persistent trend, while the empirically phase-corrected sinusoid accurately reconstructed timing and intensity. Rainfall variability is therefore best characterized by episodic realignments rather than secular drift. Embedding these diagnostics into regional early-warning and agro-climatic advisory systems can substantially improve onset and cessation forecasting. Future extensions that couple this framework with teleconnection indices will clarify the ocean–atmosphere controls on West African rainfall variability.

Declarations

Declaration of competing interest

The authors declare that there are no competing interests.

Ethics approval and consent to participate

Not applicable.

Consent for publication

Not applicable.

Availability of data and material

The dataset used and analysed during the current study is available from the corresponding author upon reasonable request.

Clinical trial number
Not applicable.

Funding
The authors received no financial support for the research, authorship, or publication of this article.

Authors' contributions
S.B-A.: Conceptualization, Validation, Methodology, Formal Analysis, Writing - Original Draft, Software, Writing - Review & Editing.
F.A.M: Visualization, Writing - Review & Editing, Investigation, Methodology. Data Collection, Data Curation,
J.A: Validation, Writing - Review & Editing, Visualization, Investigation.
F.H.A.: Visualization, Validation, Writing - Review & Editing, Investigation.

Acknowledgements: Not applicable.

REFERENCES

1. Olarewaju, O. O., Fawole, O. A., Baiyegunhi, L. J., & Mabhaudhi, T. (2025). Integrating sustainable agricultural practices to enhance climate resilience and food security in Sub-Saharan Africa: a multidisciplinary perspective. Sustainability, 17(14), 6259.
2. Omokpariola, D. O., Agbanu-Kumordzi, C., Samuel, T., Kiswii, L., Moses, G. S., & Adelegan, A. M. (2025). Climate change, crop yield, and food security in Sub-Saharan Africa. Discover Sustainability, 6(1), 678.
3. Sian, K. T. C. L. K., Ayugi, B. O., Onyutha, C., Sagero, P., & Ait Brahim, Y. (2025). Rainfall variability across Africa. In Climate Change and Rainfall Extremes in Africa (pp. 3-26). Elsevier.
4. Ayiah-Mensah, F., Bosson-Amedenu, S., Baah, E. M., & Addor, J. A. (2025). Advancements in seasonal rainfall forecasting: A seasonal auto-regressive integrated moving average model with outlier adjustments for Ghana's Western Region. Scientific African, 28, e02632.
5. Bosson-Amedenu, S., Baah, E. M., Ayiah-Mensah, F., & Addor, J. A. (2025). Advanced time series modelling to address seasonal variability and extreme rainfall in Ghana. BMC Environmental Science, 2(1), 8.
6. Adams, F., Ullah, A., Nimoh, F., Mensah, A., Quaye, J., & Kanzoni, E. (2025). Enhancing food security and livelihoods through dry season farming as a climate resilience strategy: A study in the Upper East Region of Ghana. Journal of Environmental Management, 384, 125377.
7. Dunee, D., Dagadu, P. P., Ayimadu, E. T., Asante, I. O., Daanaah, B., Galaa, M. V., & Pangestu, F. F. (2025). Impact of climate change on water resources and its implications on biodiversity, flood disasters, and food security in Ghana: a review. GeoJournal, 90(3), 1-17.
8. Kyei-Manuh, S., Osei, M. A., Aryee, J. N., Quansah, E., Obuobie, E., & Amekudzi, L. K. (2025). Lightning and thunderstorms, the source of severe weather over Ghana, West Africa. PLOS Climate, 4(9), e0000703.
9. Obuobie, E., Agyekum, J., Osei, M. A., & Addi, M. (2025). Changes in extreme precipitation events in the Volta River Basin under 1.5° C, 2° C and 3° C global warming levels. Theoretical and Applied Climatology, 156(7), 1-17.
10. Rauch, M., Bliefernicht, J., Maranan, M., Fink, A. H., & Kunstmann, H. (2025). Interannual rainfall variability in west africa: reconstruction based on atmospheric circulation patterns. International Journal of Climatology.
11. Acquaah, E. K., Mearns, K., & Agyepong, A. (2025). Using the Mann-Kendall trend analysis test to investigate the monthly and annual rainfall trends of seven locations along the Volta Lake and some tributaries.
12. Asamoah, J., Annor, T., Larbi, I., Limantol, A. M., Abiodun, B., Ansah, S. O., & Awuah, A. Spatio-Temporal Assessment of Dry Spells within the White Volta Basin of Ghana. Available at SSRN 5314570.
13. Mangara, R. J., & Limbu Sr, P. T. (2025). Spatio-temporal Dynamics of the Onset and Cessation of OND Rainy Season across Bimodal Regions of Tanzania. Tanzania Journal of Science, 51(3), 20.
14. Amoako, P. K., Tham-Agyekum, E. K., Bakang, J. E. A., Brobbey, L. K., Ankuyi, F., & Ayerakwa, M. F. (2025). Perceptions of Climate Variability among Smallholder Cocoa Farmers in Ghana. International Journal on Food, Agriculture and Natural Resources, 6(3), 30-38.
15. Worou, O. N., Govoeyi, B., Saley, I. A., Badolo, F., Traore, B., Nebie, B., & Abdoulaye, T. (2025). Perceptions and adaptation strategies: The role of climate information services among farmers in Sikasso, Mali.
16. Mishra, P., Ray, S., Lal, P., Nair, S. B., Matuka, A., Tashkandy, Y., & Emam, W. (2025). Climate modeling for South Asia: statistical and deep learning for rainfall and temperature prediction. Scientific Reports, 15(1), 38235.
17. Sapkota, N., Khattri, K. B., & Aryal, D. (2025). Modeling Precipitation: A Statistical and Machine Learning Approach. International Journal on Engineering Technology, 2(2), 188-203.
18. Banik, R., & Biswas, A. (2025). Rainfall prediction for climate-resilient agriculture: a robust ensemble with SARIMA and LightGBM. Paddy and Water Environment, 23(2), 263-275.
19. Tefera, M. L. (2025). Sustainable Solutions to Land Degradation and Rainfall Variability in Sub-Saharan Africa: Integrating Traditional Water Management, Agricultural Intensification, and Machine Learning Approaches.
20. Liu, Y., Han, Y., Zhang, Y., Luo, H., & Dong, L. (2025). Study of the Diurnally Asymmetric Precipitation Trends over Land and Ocean in a Warming Climate. Journal of Climate.

21. Chen, L., Ma, Z., & Fei, J. (2025). Investigating the effects of tropical cyclone intensity, translation speed, and environmental vertical wind shear on precipitation asymmetry. Science China Earth Sciences, 1-12.
22. Sharma, S., Ha, K. J., Rodgers, K. B., Chung, E. S., Lee, S. S., & Nellikkattil, A. B. (2025). Substantial shift in phase and amplitude of Indian rainfall beyond 2100. npj Climate and Atmospheric Science, 8(1), 236.
23. Ji, X., Feng, J., Li, J., & Zhang, Y. (2025). Distinct Hadley circulation attributable to rapid and slow El Niño decay and its regional impacts. npj Climate and Atmospheric Science, 8(1), 342.
24. Malakouti, S. M. (2025). Leveraging SHapley Additive exPlanations (SHAP) and fuzzy logic for efficient rainfall forecasts. Scientific Reports, 15(1), 36499.
25. Brennan, K. P., & Wilhelm, L. (2025). Saharan dust linked to European hail events. Atmospheric Chemistry and Physics, 25(18), 10823-10836.
26. Rogalski, C. (2025). Nonlinear Thresholds and Structural Determinants of Climate-Related Emigration: A Machine Learning Approach.
27. Bosson-Amedenu, S., Prah, K. A., Adams, F. H., Appiah, S. T., & Simons, A. (2016a). Modelling of malaria risk factors in the Mpohor District of Ghana using logistic regression. Mathematical Theory and Modeling, 6(12), 24–58.
28. Bosson-Amedenu, S., Prah, K. A., Adams, F. H., Appiah, S. T., & Simons, A. (2016b). Malaria prevalence in rural and urban communities of Mpohor District of Ghana. Mathematical Theory and Modeling, 6(12).
29. Bosson-Amedenu, S., Prah, K. A., & Adams, F. H. (2016c). Seasonal variation and trends of malaria prevalence in the Mpohor District of Ghana. Mathematical Theory and Modeling, 6(12).
30. Bosson-Amedenu, S. (2017). Nonseasonal ARIMA modeling and forecasting of malaria cases in children under five in EdumBanso Sub-district of Ghana. Asian Research Journal of Mathematics, 4(3), 1–11.
31. Bosson-Amedenu, S., Vivian, N., & Osei-Asibey, E. (2019). Statistical analysis of trends of malaria diagnosis and patient demographics: A multivariate study of clinic data in Ghana. American Journal of Computational and Applied Mathematics, 9(2), 43–49.*
32. Wood, S. N. (2017). Generalized additive models: an introduction with R. chapman and hall/CRC.
33. Wood, S. N. (2024). Generalized additive models. Annual Review of Statistics and its Application, 12.
34. Le Roy, E. J., & Ummenhofer, C. C. (2025). Past and future modulation of the ENSO teleconnection to Southeast Asian rainfall by interbasin interactions. Geophysical Research Letters, 52(4), e2024GL111916.
35. Choudhari, N., Jacob, B. G., Elshorbany, Y., & Collins, J. (2025). Unveiling Asymptotic Behavior in Precipitation Time Series: A GARCH-Based Second Order Semi-Parametric Autocorrelation Framework for Drought Monitoring in the Semi-Arid Region of India. Hydrology, 12(10), 254.
36. Onyia, A. N., & Ijomah, J. O. (2025). MONITORING THE DYNAMICS AND ENVIRONMENTAL EFFECTS OF WEST AFRICAN LINE SQUALL USING SATELLITE IMAGERIES. Irish Journal of Environment and Earth Sciences, 9(6), 1-17.

Supplementary diagnostics: Spectral, autocorrelation, and clustering evidence (Supplementary Figures S18–S23)

To support and cross-validate the main results, this study provides a compact suite of diagnostics—spectral, temporal-dependence, and shape-based clustering—demonstrating that Western Ghana's rainfall variability from 2017–2023 is governed by a seasonal phase structure and amplitude modulation rather than strong month-to-month memory or monotonic trends. Detailed interpretations are provided below; figure panels are provided in Supplementary Figures S18–S23.

Clustered heatmap of monthly profiles (k-means on standardized months; corresponds to former

Three recurrent seasonal "shapes" summarize the period: Cluster 1 (2022–2023) shows flattened bimodality (subdued core-monsoon months); Cluster 2 (2019) shows an intense first (May–June) peak with a weaker short-rain peak; and Cluster 3 (2017–2018, 2020–2021) resembles canonical bimodality with a stronger second peak (Sep–Oct) in some years. These transitions indicate **nonlinear phase shifts** across years rather than uniform rescaling of totals.

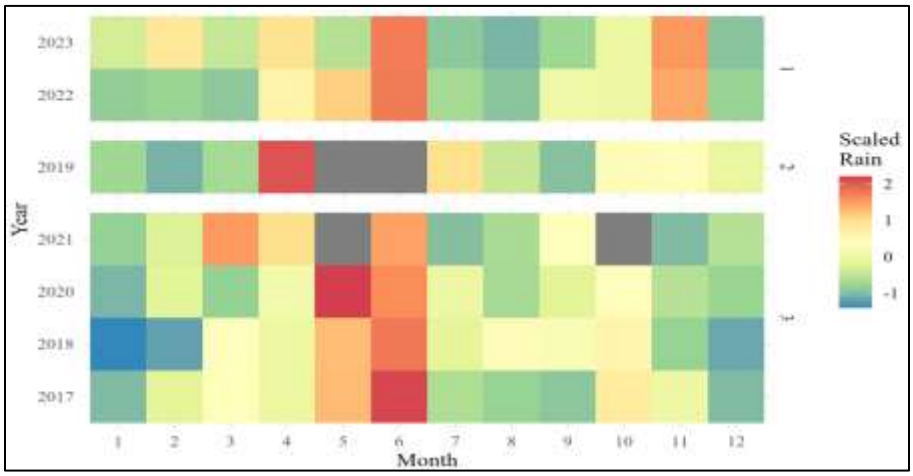

Figure S18. Clustered heatmap of recurrent seasonal patterns

S19. Wavelet power spectrum

The power is concentrated at ~1 and ~2 cycles per year, confirming dominant annual and semiannual periodicities. The broad biannual lobe indicates time-localized modulation of the second peak's strength—consistent with cluster switching between "strong long rains + weak short rains" (e.g., 2019) and "flattened" seasons **(2022–2023).**

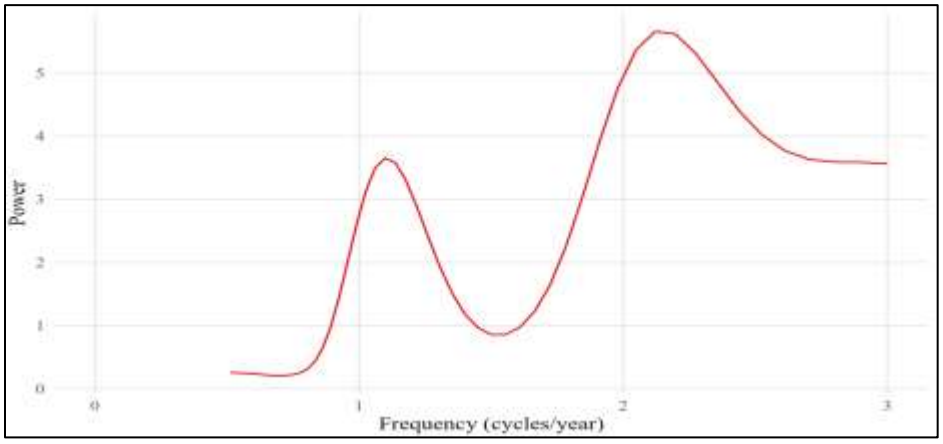

FigureS 19. Wavelet power spectrum showing annual and semiannual cycles

S20. Fourier spectrum

The distinct spikes near cycles 1 and 2/year corroborate the annual/biannual harmonics observed in S19. The variation in the ~2 cycles/year peak height aligns with the **stability or weakening of the short-rain peak**, helping explain cluster differences across years.

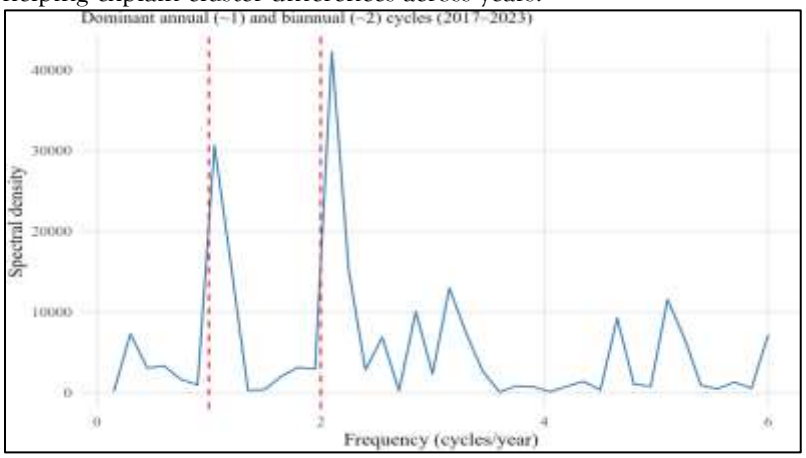

Figure 20. Fourier Spectrum indicating Annual and Biannual Harmonics

S21. Rolling skewness

Skewness is mostly positive and often >1.0 (e.g., 2019–2020), indicating right-tailed monthly distributions with occasional large events. Temporary dips (2018, 2021) align with drier baselines; rebounds thereafter explain sporadic large positive deviations in model residuals—i.e., extremes are distributional features, not noise.

S22. Rolling variance

Variance surges approximately 2020 and again after 2022 indicate **heightened volatility** in monthly totals. The lower-variance windows near 2018 and 2021 flank these surges and match the STL minima and cluster shifts. The post-2022 increase implies **wider intermonthly swings**, even when annual totals are unexceptional—relevant for water and farm planning.

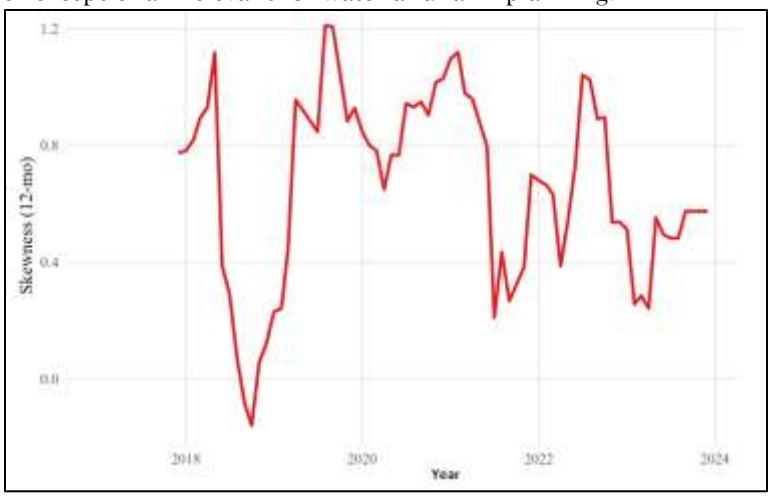

Figure 23. Rolling Variance and Skewness Showing Interannual Volatility

S23. Partial autocorrelation function (PACF) of monthly rainfall

The small but noticeable short-lag structure (lag 1; seasonal lags ~11–12) is consistent with short-memory plus seasonal dependence. Negative partial correlations at intermediate lags suggest overcorrection after peaks (alternating wet/dry transitions). This favours cyclic month terms in the GAM and cautions against purely long-memory formulations.

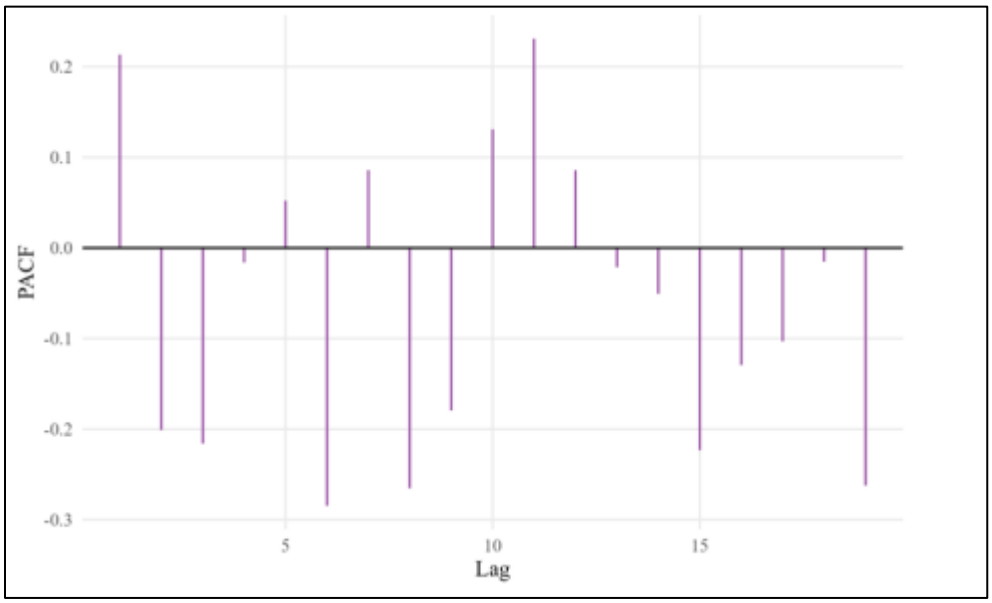

Figure22. **Partial autocorrelation function indicating seasonal dependence**

S24. Autocorrelation function (ACF) of monthly rainfall.

Lag-1 autocorrelation is modest (~0.22), and alternating signs at intermediate lags reflect compensatory wet–dry reversals. Re-emergent positives near 12 months indicate annual periodicity. Overall, weak short-term memory supports seasonal smooths rather than AR terms in the main GAM.

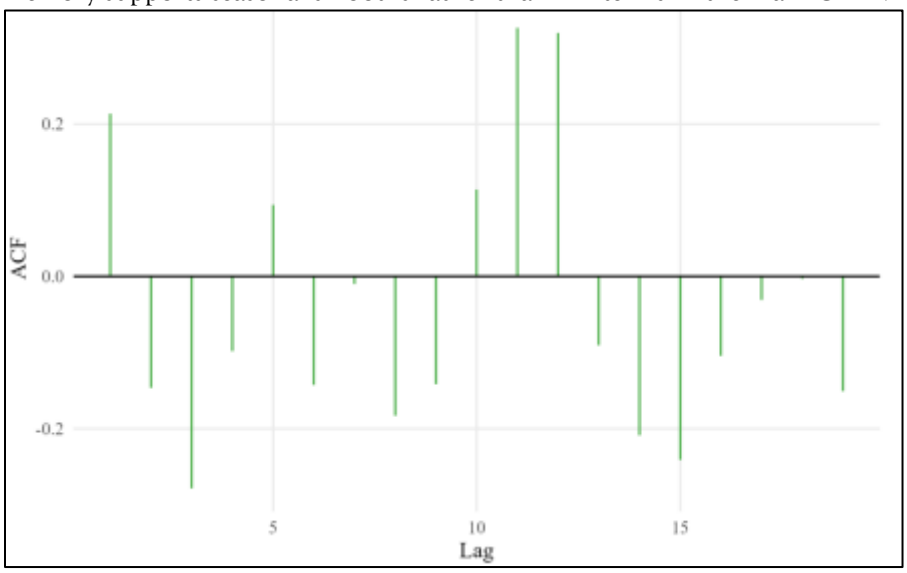

Figure 23. Autocorrelation Function Showing Weak Short-Term Memory

S25. Dynamic time warping (DTW) dendrogram of rainfall patterns

Hierarchical clustering of monthly profiles reveals interannual regimes: 2018–2021 cluster closely; 2022–2023 pair moderately; 2019 and 2020 are distant outliers (DTW heights >800), reflecting distinct phase/amplitude structures—2019 wetter/more symmetric; 2020 compressed the main season. The early series distinctiveness of 2017 suggests a transitional pattern. DTW confirms that rainfall variability is organized (regime-like) rather than random.

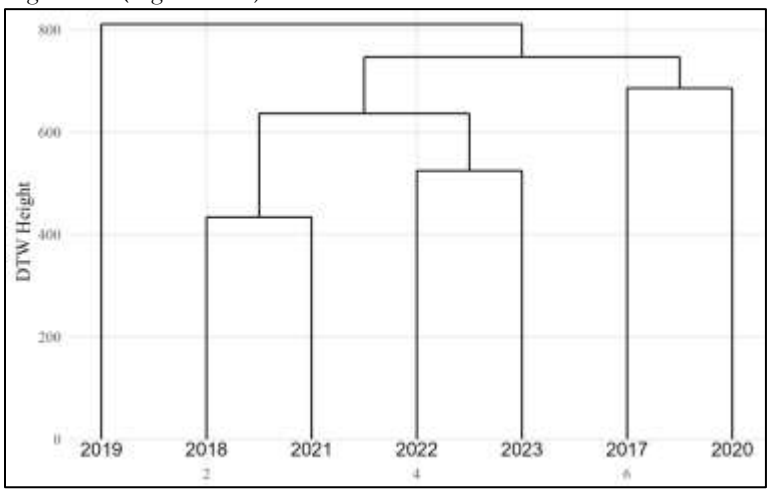

FigureS 25. DTW-Based Dendrogram of Rainfall Patterns for Interannual Phase Shifts